Accelerated convergence via adiabatic sampling for adsorption and desorption processes

Caroline Desgranges*

Department of Physics & Applied Physics,

University of Massachusetts, Lowell, MA 01854, USA

Jerome Delhommelle†

Department of Chemistry, University of Massachusetts, Lowell, MA 01854, USA

(Dated: January 31, 2025)

* Co-corresponding author. Electronic mail: caroline_desgranges@uml.edu

† Co-corresponding author. Electronic mail: jerome_delhommelle@uml.edu

Abstract

Under isothermal conditions, phase transitions occur through a nucleation event when conditions are sufficiently close to coexistence. The formation of a nucleus of the new phase requires the system to overcome a free energy barrier of formation, whose height rapidly rises as supersaturation decreases. This phenomenon occurs both in the bulk and under confinement, and leads to a very slow kinetics for the transition, ultimately resulting in hysteresis, where the system can remain in a metastable state for a long time. This has broad implications, for instance, when using simulations to predict phase diagrams or screen porous materials for gas storage applications. Here, we leverage simulations in an adiabatic statistical ensemble, known as adiabatic grand-isochoric ensemble (μ, V, L) ensemble, to reach equilibrium states with a greater efficiency than its isothermal counterpart, *i.e.*, simulations in the grand-canonical ensemble. For the bulk, we show that at low supersaturation, isothermal simulations converge slowly while adiabatic simulations exhibit a fast convergence over a wide range of supersaturation. We then focus on adsorption and desorption processes in naoporous materials, assess the reliability of (μ, V, L) simulations on the adsorption of Argon in IRMOF-1, and demonstrate the efficiency of adiabatic simulations to predict efficiently the equilibrium loading during the adsorption and desorption of Argon in MCM-41, a system that exhibits significant hysteresis. We provide quantitative measures of the increased rate of convergence when using adiabatic simulations. Adiabatic simulations explore a wide temperature range, leading to a more efficient exploration of the configuration space.

I. INTRODUCTION

Systems undergoing a first-order phase transition often exhibit hysteresis. This behavior can be characterized as a delay in the transition process. Such a lag is further enhanced when the conditions are close to the temperature at coexistence. Rather than transitioning directly to the thermodynamically stable phase, the system can remain in a metastable state for a significant amount of time[1]. In single-component systems, this is, for instance, the case for a supercooled liquid prior to the formation of the stable crystal phase or of a supersaturated vapor prior to the onset of the stable liquid phase[2,3]. The phenomenon of hysteresis can be traced back to the large free energy barrier associated with the nucleation of the new, thermodynamically stable, phase. Theories, like the classical nucleation theory (CNT), account for the existence of this free energy barrier under isothermal conditions[1]. CNT shows that this barrier is due to a competition between a favorable free energy contribution, arising from the conversion of the metastable phase into the stable phase, and an unfavorable free energy contribution, arising from the creation of an interface between the metastable and the stable phase. This result applies to the bulk, but also to nanoconfined systems for adsorption and desorption processes under subcritical conditions[4–12]. This has prompted the development of advanced sampling simulation strategies including, among others, umbrella sampling[2,3], Wang-Landau sampling[13–15], or transition-matrix methods[16,17]. These methods allow the system to overcome free energy barriers, enabling the simulation of the phase transition process and providing direct access to the transition pathway. The success of these methods, most notably of the flat-histogram methods, relies on the extensive sampling of the configuration space and thus requires generating a very large number of configurations. Implementing these detailed and computationally intensive simulation methods can become unpractical in many practical cases such as, for instance, when performing a high-throughput screening of nanoporous materials for gas storage applications[18–26].

There is therefore a need for a robust and efficient method that provides a direct and rapid access to the equilibrium limit, *i.e.*, the equilibrium phase diagram for the bulk or the equilibrium value for the loading when studying the adsorption of a fluid in a nanoporous material. Since the issue can be traced back to the existence of free energy barriers that are difficult to overcome under isothermal conditions, performing simulations in an adiabatic ensemble[27–29] has emerged as a promising option[30–34]. For instance, recent work using

either the adiabatic grand-isochoric (μ, V, L) ensemble[35,36] and the adiabatic grand-isobaric ensemble (μ, P, R) ensemble[37,38] has recently been applied to determine bulk phases of single-component systems[39–41] and mixtures[42]. To our knowledge, simulations in adiabatic ensembles have focused so far on bulk phases and have not been extended yet to explore adsorption in confined systems. Furthermore, an assessment of their efficiency relative to simulations in the corresponding isothermal ensemble is needed to establish their potential usefulness in screening protocols. In this work, we focus on the case of simulations performed in the adiabatic grand-isochoric (μ, V, L) ensemble and on the corresponding isothermal ensemble, *i.e.*, the grand-canonical (μ, V, T) ensemble. The aim of this work is two-fold. First, we extend the use of simulations in the (μ, V, L) ensemble for fluid adsorption in nanoporous materials. To achieve this, we study an adsorption process under supercritical conditions, *i.e.*, a system for which there is no free energy barrier under isothermal conditions and show that (μ, V, L) and (μ, V, T) simulations give results in excellent agreement with each other. Second, we assess the efficiency of adiabatic simulations through a systematic comparison with isothermal simulations for subcritical systems, both in the bulk and under nanoconfinement. In the bulk, we show that the convergence rate of adiabatic simulations is essentially independent of the degree of supersaturation, while the convergence rate of isothermal simulations rapidly increases as the degree of supersaturation decreases, exhibiting a behavior expected for an activated process. We show that a similar behavior takes place under nanoconfinement for high enough degrees of supersaturation. For a low supersaturation, we find that isothermal simulations exhibit a strong hysteresis and remain in metastable states over the entire course of the simulations, while adiabatic simulations converge towards the equilibrium state. We show that this behavior can be traced back to the ability of adiabatic simulations to sample a wide range of temperature and potential energy, thereby enabling the efficient exploration of the configuration space and the faster convergence of adiabatic simulations.

The paper is organized as follows. We first present the adiabatic formalism and how simulations are implemented in the adiabatic grand-isochoric (μ, V, L) ensembles. We then discuss the potential models used for Argon and for the two nanoporous materials (IRMOF-1 and MCM-41) considered in this work. Section IV consists of a discussion of the results obtained in this work, starting with a comparison of adiabatic and isothermal simulations of the onset of the liquid (bulk) phase of Argon, followed by the validation of (μ, V, L) simulations to model the supercritical adsorption of Argon in IRMOF-1. We then examine

the adsorption (condensation) and desorption (evaporation) process in a MCM-41 capillary, a system known to exhibit hysteresis, to assess the efficiency of adiabatic simulations and their ability to access the equilibrium value for the loading under conditions that lead to hysteresis in isothermal simulations. We finally draw the main conclusions from this work in Section V.

II. FORMALISM

Isothermal ensembles are in thermal contact with a reservoir, allowing for the system's temperature T to remain constant, and equal to that of the reservoir, through heat exchanges between the system and the reservoir[43,44]. On the other hand, adiabatic ensembles are thermally insulated from their surroundings[27,28]. This means that energy heat exchanges are prevented, although other types of energy exchanges may still occur. As a result, temperature is allowed to change and another function, known as heat function, remains constant in adiabatic ensembles[28,38].

As discussed by Graben and Ray[38], isothermal and adiabatic ensembles can be seen as pairs of ensembles whose thermodynamic potentials are related to each other by Legendre transforms[45]. An example of such a pair are the canonical ensemble (N, V, T) and microcanonical ensemble (N, V, E), whose thermodynamic potentials are related through

$$A(N, V, T) = E - TS(N, V, E) \tag{1}$$

Here the internal energy E plays the role of heat function, the Helmholtz energy $A(N, V, T)$ is the thermodynamic potential for the (N, V, T) ensemble, and the entropy $S(N, V, E)$ denotes the thermodynamic potential for the (N, V, E) ensemble.

In this work, we focus the isothermal-adiabatic pair of ensembles that allows for changes in the number of particles in a system with a constant volume. This pair[28,44,46] involves the well-known grand-canonical ensemble (μ, V, T) and the adiabatic grand-isochoric (μ, V, L) ensemble[33,35,36,41,47–49]. The thermodynamic potentials for the two ensembles are related through

$$J(\mu, V, T) = L - TS(\mu, V, L) \tag{2}$$

where the heat function L is the Hill energy defined as

$$L = E - \mu N \tag{3}$$

and where the functions $J(\mu, V, T)$ and $S(\mu, V, L)$ are the thermodynamic potentials for the grand-canonical and grand-isochoric adiabatic ensemble, respectively.

In an adiabatic ensemble[28,37,39,40,42,49], the thermodynamic potential S can be written as a function of the phase space volume through

$$S = k_B \log \Omega \tag{4}$$

This relation applies to the microcanonical ensemble (N, V, E), isobaric-isoenthalpic ensemble (N, P, H), grand-isobaric adiabatic ensemble (μ, P, R), and to the grand-isochoric adiabatic ensemble (μ, V, L) we examine in this work. We add for completeness that alternative definitions for the entropy using the density of states ω instead of Ω have been shown to provide equivalent results in the thermodynamic limit[40,50].

In the (μ, V, L) ensemble, the phase space volume can be obtained by performing the following multi-dimensional integral

$$\Omega(\mu, V, L) = \sum_{N=0}^{\infty} \frac{1}{N! h^{3N}} \int ... \int \Theta\left(L + \mu N - \mathcal{H}\right) d\mathbf{r}^{3N} d\mathbf{p}^{3N} \tag{5}$$

where Θ denotes the Heaviside function, $d\mathbf{r}^{3N}$ and $d\mathbf{p}^{3N}$ indicates that the integration is performed over the $3N$ position and momenta coordinates for the N particles of the system, $\mathcal{H} = K + U$ is the Hamiltonian for the N-particle system.

$\Omega(\mu, V, L)$ can then be evaluated using Laplace-transform techniques[42,49,51] to provide the following equation

$$\Omega(\mu, V, L) = \sum_{N=0}^{\infty} \frac{1}{N! h^{3N}} \frac{(2\pi m)^{3N/2}}{\Gamma(\frac{3N}{2} + 1)} \int ... \int \left(L + \mu N - U\right)^{3N/2} \Theta\left(L + \mu N - U\right) d\mathbf{r}^{3N} \tag{6}$$

After performing the variable change $q_i = r_i / V^{1/3}$ to make the position coordinates dimensionless, we obtain

$$\Omega(\mu, V, L) = \sum_{N=0}^{\infty} \frac{1}{N! h^{3N}} \frac{(2\pi m)^{3N/2}}{\Gamma(\frac{3N}{2} + 1)} \int ... \int V^N \left(L + \mu N - U\right)^{3N/2} \Theta\left(L + \mu N - U\right) d\mathbf{q}^{3N} \tag{7}$$

The density of states $\omega(\mu, V, L)$ can then be obtained by differentiating $\Omega(\mu, V, L)$ with respect to L as

$$\omega(\mu, V, L) = \sum_{N=0}^{\infty} \frac{(2\pi m)^{3N/2}}{N! h^{3N} \Gamma(\frac{3N}{2})} \int ... \int V^N \left(L + \mu N - U\right)^{3N/2 - 1} \Theta\left(L + \mu N - U\right) d\mathbf{q}^{3N} \tag{8}$$

The density of states can then be used to determine the weight factors involved in the Metropolis acceptance rules[29,42,49]. Specifically, the general acceptance rule for a move from an "old" configuration, denoted by o and associated with a weight factor W_o, to a "new" configuration, denoted by n and associated with a weight factor W_n, can be written as

$$acc(o \rightarrow n) = \left(1, \frac{W_n}{W_o}\right) \tag{9}$$

with, for instance, the following expression for the weight factor W_o extracted from the density of states as

$$W_o = \frac{(2\pi m)^{3N_o/2}}{N_o! h^{3N_o} \Gamma(\frac{3N_o}{2})} V_o^N \left(L + \mu N_o - U_o\right)^{3N_o/2-1} \tag{10}$$

in which N_o and U_o denote the number of particles and potential energy for the old configuration o.

This leads to the following acceptance rules for the three types of Monte Carlo moves involved in the sampling of the (μ, V, L) ensemble. For the translation ($N_o = N_n = N$), the acceptance rule is given by

$$acc(o \rightarrow n) = \left(1, \left(\frac{L + \mu N - U_n}{L + \mu N - U_o}\right)^{3N/2-1}\right) \tag{11}$$

For the insertion of a particle ($N_n = N_o + 1$), the acceptance rule becomes

$$acc(o \rightarrow n) = \left(1, \frac{(2\pi m)^{3/2} V \Gamma(\frac{3N_o}{2})}{(N_o+1) h^3 \Gamma(\frac{3(N_o+1)}{2})} \times \frac{\left(L + \mu(N_o+1) - U_n\right)^{(3(N_o+1)/2)}}{\left(L + \mu N_o - U_o\right)^{3N_o/2-1}}\right) \tag{12}$$

and the acceptance rule for the deletion of a particle ($N_n = N_o - 1$) is given by

$$acc(o \rightarrow n) = \left(1, \frac{N_o h^3 \Gamma(\frac{3N_o}{2})}{(2\pi m)^{3/2} V \Gamma(\frac{3(N_o-1)}{2})} \times \frac{\left(L + \mu(N_o-1) - U_n\right)^{(3(N_o-1)/2)}}{\left(L + \mu N_o - U_o\right)^{3N_o/2-1}}\right) \tag{13}$$

III. SIMULATION PROTOCOLS AND MODELS

A. Relation between (μ, V, T) and (μ, V, L) simulations

We carry out Monte Carlo (MC) simulations in the grand-canonical (μ, V, T) ensemble and in the grand-isochoric adiabatic (μ, V, L) ensemble for bulk Ar, as well as for Ar adsorbed in IRMOF-1 and in MCM-41. There are 3 different types of MC moves in both types of simulations: (i) random translation of an Ar atom (50% of the MC moves), (ii) insertion

of an additional Ar atom at a randomly selected position in the system (25 % of the MC moves), and (iii) deletion of a randomly selected Ar atom from the system (25 % of the MC moves). The two ensembles and thus the two types of simulations share the same (μ, V), which means that we only need to identify the $L \leftrightarrow T$ correspondence to define equivalent sets of (μ, V, L) and (μ, V, T) simulations. The average Hill energy $\langle L \rangle$ can be evaluated directly during (μ, V, T) simulations according to

$$\langle L \rangle = \langle U \rangle + \frac{3}{2} \langle N \rangle k_B T - \mu \langle N \rangle \tag{14}$$

where U denotes the potential energy of the system and $\frac{3}{2} \langle N \rangle k_B T$ is the kinetic energy for an atomic fluid. Similarly, the average temperature of the system $\langle T \rangle$ can be evaluated during a (μ, V, L) simulation according to the following equation

$$\langle T \rangle = \frac{L - \langle U \rangle + \mu < N >}{3/2 \langle N \rangle k_B} \tag{15}$$

Averages reported in the next section were collected over simulations of 10^9 MC steps. Simulations were carried out using an in-house Monte Carlo code. We provide below the equations and parameters used to model the interactions for each of the systems examined in this work.

B. Argon

We model Argon as point particles interacting through a Lennard-Jones interaction pair potential. The potential energy $U_{LJ}(r_{ij})$ between two atoms i and j is given by

$$U_{LJ}(r_{ij}) = 4\epsilon \left[\left(\frac{\sigma}{r_{ij}} \right)^{12} - \left(\frac{\sigma}{r_{ij}} \right)^{6} \right] \tag{16}$$

where r_{ij} denotes the distance between i and j, ϵ denotes the well-depth for the interaction, and σ the exclusion diameter. We use the following values[9,52] for the two Lennard-Jones parameters $\sigma = 3.4$ Å and $\epsilon/k_B = 119.8$ K. In simulations of bulk liquid Ar, the volume of the system is equal to $V = 512\sigma^3$ and periodic boundary conditions are applied in all 3 directions. Interactions between Argon atoms are calculated explicitly up to a distance of 2.5σ with the conventional long-range corrections applied beyond the cutoff distance[53].

C. Adsorption in IRMOF-1

In recent years, metal-organic frameworks[20,54–59] and covalent organic frameworks[60,61] have emerged as high-performance nanoporous materials for the storage of light gases[62,63] including, among others, carbon dioxide[14,64–67], hydrogen[19,60,63,68], noble gases[22,69,70], methane and other light hydrocarbons[21,23,71–76]. Following previous simulation studies of adsorption in IRMOF-1[15,65,66,69], we model the IRMOF-1 structure as a rigid cubic structure with a lattice constant of 25.832 Å and atomic coordinates as provided by Yaghi *et al.*[55]. We add that the approximation of considering the structure to be rigid was validated for the simulation of adsorption isotherms for light gases in previous work by Greathouse *et al.*[69]. In line with prior work[15,65,66], we model the IRMOF-1 structure with the DREIDING force field[77], whose accuracy for the prediction of adsorption isotherms has been established in previous simulation studies[62,63,78]. All interactions between Ar atoms from the adsorbed fluid and the atoms from the IRMOF-1 structure are thus modeled with Lennard-Jones potentials, and the parameters for the interactions between unlike sites are calculated according to the Lorentz-Berthelot combining rules[79].

D. Adsorption and Desorption in MCM-41

We then model the adsorption and desorption of Argon in a cylindrical pore of 10 atomic diameters, aligned with the z-axis and with a length, or lateral dimension, denoted by L_z. The functional form and parameters for the Lennard-Jones model for Argon ($\sigma = 3.4$ Å and $\epsilon/k_B = 119.8$ K) and for the nanopore are chosen so as to model a MCM-41 silica mesoporous molecular sieve and taken from prior work[5,9,80]. The interactions between the adsorbed Argon atoms and the nanopore are thus modeled with the following functional form[5,52,81,82]

$$U_{sf}(r,R) = \pi^2 \rho_s \epsilon_{sf} \sigma_{sf}^2 \left\{ \frac{63}{32} \left[\frac{R-r}{\sigma_{sf}} \left(1+\frac{r}{R}\right) \right]^{-10} F\left[-\frac{9}{2},-\frac{9}{2};1;\left(\frac{r}{R}\right)^2\right] - 3\left[\frac{R-r}{\sigma_{sf}} \left(1+\frac{r}{R}\right) \right]^{-4} F\left[-\frac{3}{2},-\frac{3}{2};1;\left(\frac{r}{R}\right)^2\right] \right\} \tag{17}$$

in which r is the radial coordinate of the Ar atom adsorbed in the pore, R is the pore radius (here 5σ), ρ_s is the surface density of adsorption centers and $F(\alpha,\beta;\gamma;\delta)$ is the hypergeometric series. The parameters for the solid-fluid interactions were taken as $\rho_s \epsilon_{sf} = 2253$ K/nm^2 and $\sigma_{sf} = 3.17$ Å. This functional form accurately models the interaction

between adsorbate and the structureless cylindrical layer of adsorption centers on the pore wall[83]. We carry out simulations of capillary condensation and evaporation in nanopores with a long lateral dimension $L_z = 30\sigma$ to allow for the sampling of symmetry breaking configurations containing bubbles and liquid bridges[5,9,10]. Periodic boundary conditions are applied along this lateral direction z. We also calculate explicitly the interactions between Argon atoms up to a distance of 5σ and neglect the fluid-fluid interactions beyond that cutoff distance. Finally, for this series of results, we report results in terms of units reduced with respect to the Lennard-Jones parameters and mass of Argon to facilitate the comparison with prior work.

IV. RESULTS AND DISCUSSION

A. Argon

We first comment on the results obtained for the bulk. We start by examining the dependence of L as a function of T and how a correspondence between (μ, V, T) and (μ, V, L) simulations can be established. The top left graph in Fig. 1 shows a comparison between results obtained during (μ, V, T) and (μ, V, L) simulations for Argon at $\mu = -230$ kJ/kg. As discussed above, gradually increasing the imposed value for the Hill energy in (μ, V, L) simulations results in a quasi-linear increase in the average temperature $\langle T \rangle$ given by Eq. 15 as shown by the plot. Moreover, we find that an input value of $L/k_B = 2.356 \times 10^5$ K results in an average temperature $\langle T \rangle = 93.64$ K. We confirm this result by carrying out a (μ, V, T) simulation for the state point studied here ($\mu = -230$ kJ/kg, $T = 93.64$ K) and calculating the value taken by $\langle L \rangle$ using Eq. 14. The match observed for the two types of simulations extends to other properties as shown for the number of atoms in the top right graph in Fig. 1, which shows that the two types of simulations sample configurations corresponding to the same state point. The bottom left plot in Fig. 1 extends these findings to a wider range of μ at $T = 93.64$ K and shows that an excellent agreement is obtained between the results obtained with the two types of simulations for the dependence of the Hill energy as a function of μ. Furthermore, we provide a comparison between (μ, V, T) and (μ, V, L) simulation results for the dependence of density on μ at two different temperatures ($T = 93.64$ K and $T = 120$ K) and obtain again an excellent agreement between the results

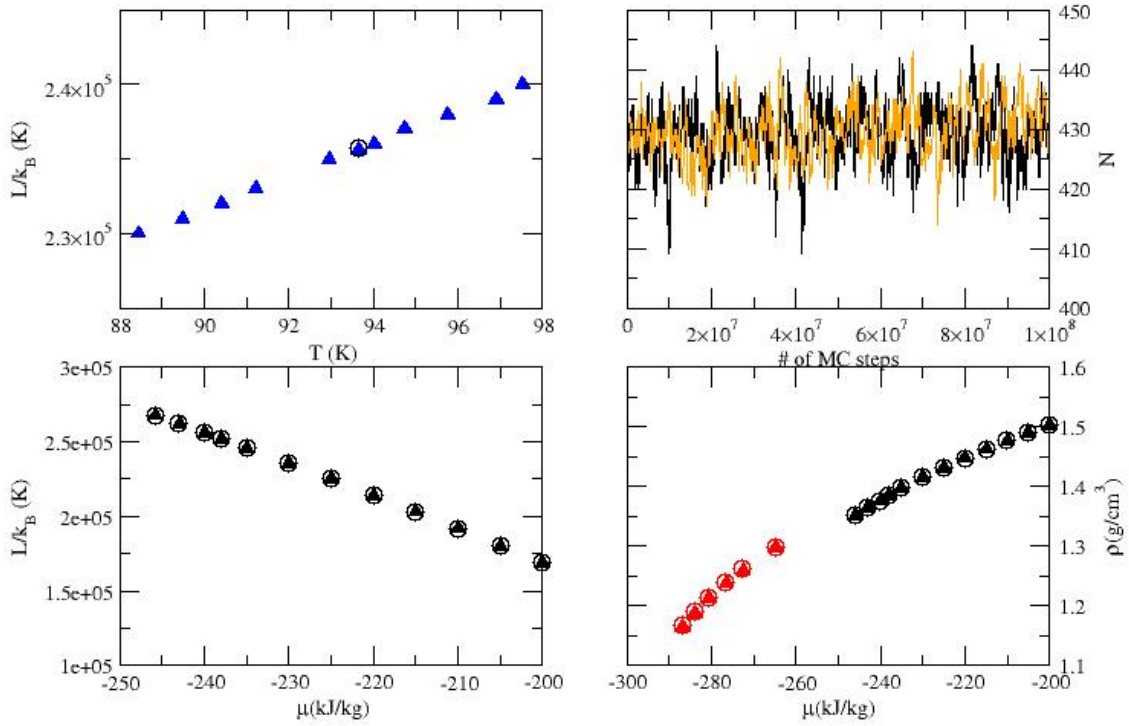

FIG. 1: (Top Left) Argon at $\mu = -230$ kJ/kg. Hill Energy L vs. temperature T for a series of (μ, V, L) simulations for increasing L values (filled triangles) and for a (μ, V, T) simulation at $T =$ 93.64 K (open circle). (Top Right) Argon at $\mu = -230$ kJ/kg. Comparison between the number of Argon atoms after the simulations have converged for a (μ, V, L) simulation with $L = 2.356 \times 10^5$ and a (μ, V, T) simulation at $T = 93.64$ K. (Bottom Left) Argon at $T = 93.64$ K. Variation of L as a function of μ for a series of (μ, V, T) simulations (open circles) and the corresponding (μ, V, L) simulations (filled triangles). (Bottom Right) Density ρ vs μ at $T = 93.64$ K (black) and $T = 120$ K (red) obtained with (μ, V, L) simulations (filled triangles) and a (μ, V, T) simulations (open circles)

obtained with both methods.

The next step consists in comparing the performance of the two methods for state points that are closer to coexistence and thus more susceptible to a delayed onset of the phase transition process. We focus on the results obtained at $T = 120$ K for which the chemical

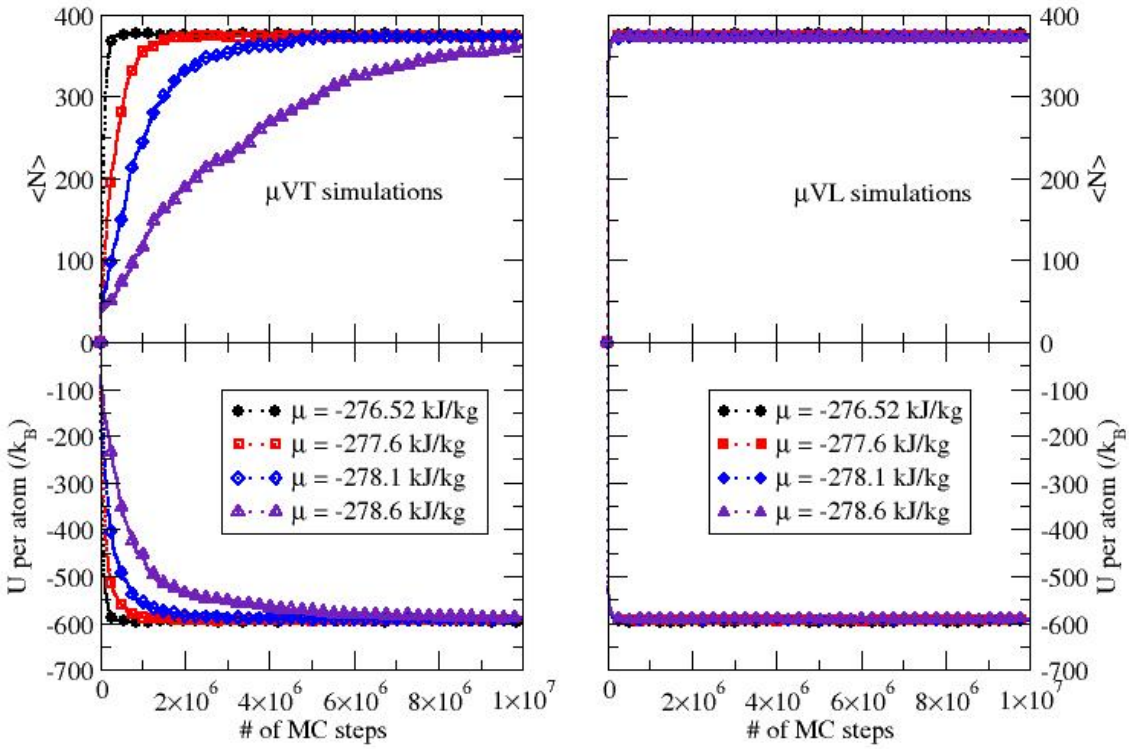

FIG. 2: Average number of atoms (top) and average potential energy per particles (bottom) in bulk Ar at $T = 120$ K collected over 200 realizations of MC runs of 10^7 MC steps each. The left panel shows results obtained for simulations in the (μ, V, T) ensemble while the right panel shows results for the corresponding (μ, V, L) simulations. The plots show that the rate at which (μ, V, T) converge decrease as the conditions approach coexistence ($\mu = -287.3$ kJ/kg) while convergence is reached within the first 5×10^5 MC steps of the (μ, V, L) simulations for all conditions.

potential at the vapor-liquid coexistence is $\mu_{coex} = -287.3$ kJ/kg for the model[14,16]. We examine the number of MC steps necessary to reach convergence for both types of simulations over many realizations. Each realization is defined as a new set of initial conditions, *i.e.*, here, an empty simulation cell ($N = 0$) and a different seed, and thus sequence, for the generation of the random numbers used in the simulations. We carry out simulations at a given temperature ($T = 120$ K) and selected chemical potentials, ranging from $\mu =$

-276.52 kJ/kg to $\mu = -278.6$ kJ/kg, both in the (μ, V, T) and (μ, V, L) ensembles. In the latter, we fine-tune for each μ the value of the Hill energy L so that the average temperature matches the temperature of 120 K used in the (μ, V, T) simulations. The average number of atoms and average potential energy are plotted against the number of MC steps for each set of conditions and each type of simulations. During the (μ, V, T) simulations, as the chemical potential decreases and approaches the chemical potential at coexistence, the number of MC steps necessary for filling the box and obtaining the liquid phase becomes larger and larger. For instance, it takes on average 5×10^5 MC steps to converge at $\mu = -276.52$ kJ/kg while it takes 1.8×10^6 MC steps to converge when the chemical potential decreases to $\mu = -277.6$ kJ/kg and more than 10^7 MC steps when $\mu = -278.6$ kJ/kg. On the other hand, Fig. 2 shows that convergence is reached within the first 5×10^5 MC steps of the (μ, V, L) simulations for all μ values. This is evidenced by both the average number of atoms in the system (top panels) and the average potential energy per atom (bottom panels). This points to a much faster convergence of the $(\mu, V.L)$ simulations as conditions approach coexistence.

To better understand the reason for the increased efficiency of the adiabatic simulations, we turn to the computation of the average temperature of the system using Eq. 15 and plot its variation as a function of the number of MC steps in the left panel of Fig. 3. For all conditions, the results show that the average temperature of the system takes very large values at the beginning of the simulations before undergoing a steady decrease towards the equilibrium value of 120 K. This is a major difference with how configurations are sampled during a (μ, V, T) simulation, where the temperature is kept constant at the equilibrium value and the system has to overcome a free energy barrier close to coexistence. We explore this point further by showing N_τ the characteristic number of MC steps for convergence in the right panel of Fig. 3. To obtain N_τ, we fit the change in the average number of atoms $\langle N \rangle$, averaged over all realizations, as a function of N_{MC} the number of MC steps with the following functional form

$$\langle N \rangle = N_\infty \left[1 - \exp\left(\frac{N_{MC}}{N_\tau} \right) \right] \tag{18}$$

in which N_∞ denotes the number of atoms in the system when the simulation has converged. The results obtained for the (μ, V, L) and (μ, V, T) simulations are shown in the right panel of Fig. 3 as a function of the supersaturation $\Delta\mu = \mu - \mu_{coex}$. N_τ exhibits a markedly different behavior for the two types of simulations. In the case of (μ, V, T) simulations, N_τ

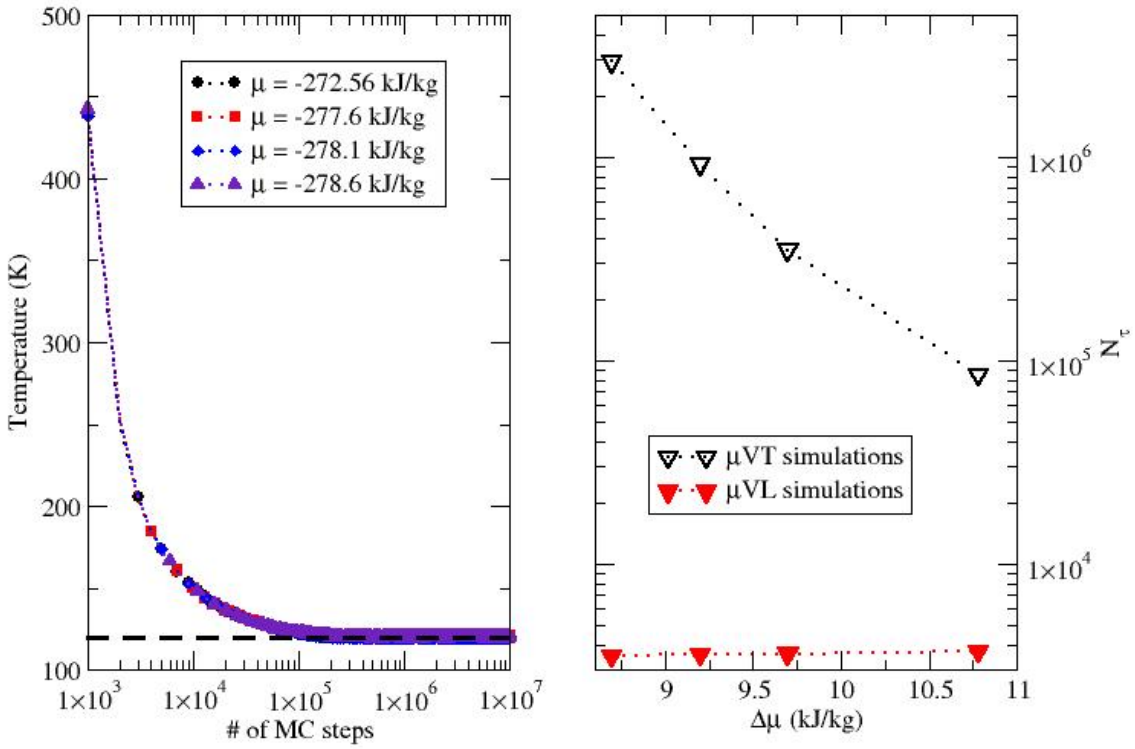

FIG. 3: (Left) Average temperature in bulk Ar collected over 200 realizations of MC runs with 10^7 MC steps for the μVL simulations (same conditions as in Fig. 2). The dashed line indicates the equilibrium temperature of 120 K towards which all simulations converge. In the early stages of the simulation, the average temperature overshoots the equilibrium value thereby ensuring a faster equilibration than for (μ, V, T) simulations. (Right) Characteristic number of MC steps N_τ against the supersaturation $\Delta\mu = \mu - \mu_{coex}$. For (μ, V, T) simulations, N_τ increases as conditions approach coexistence and $\Delta\mu$ decreases. On the other hand, in μVL simulations, N_τ remains constant over the entire $\Delta\mu$ range.

increases rapidly as the supersaturation decreases as expected with all nucleation-controlled events which require the system to overcome a free energy barrier[1–3]. On the other hand, N_τ remains quasi-constant over the range of supersaturation studied here. This behavior is consistent with the absence of any barrier under adiabatic conditions and accounts for the

increased efficiency of (μ, V, L) simulations as the conditions approach coexistence.

B. Adsorption in IRMOF-1

We now examine the adsorption of Argon in IRMOF-1. First, since prior (μ, V, L) simulation studies have focused on bulk phases so far[35,36,41,47–49], we provide an assessment of the method on a "simple" case, *i.e.* the adsorption of Argon under supercritical conditions at $T = 150$ K and $T = 200$ K. This means that, since there are no free energy barriers involved and thus no hysteresis in this case, we can carry out a validation of the (μ, V, L) simulation method for adsorption processes by comparing the results so obtained to the corresponding (μ, V, T) simulation results.

Fig. 4 shows a summary of the results obtained during both sets of simulations, together with results obtained in prior work using a flat-histogram method[15]. For both (μ, V, T) and (μ, V, L) simulations, gradually increasing the imposed value for μ results in an increase in the number of atoms adsorbed in IRMOF-1. As with the (μ, V, L) simulations for the bulk, we fine-tune the value of L for a given μ to obtain an average temperature $< T >$ equal to either 150 K or 200 K. Fine-tuning L allows us to match the temperature T used in isothermal simulations or experiments and, as a result, enables a direct comparison with the adsorption and desorption branches obtained under isothermal conditions. Examples of snapshots of the configurations so obtained show an unit cell for IRMOF-1, together with the adsorbed Argon atoms, obtained at different stages of the loading process during (μ, V, L) simulations at $T = 150$ K. To facilitate comparison with other work, we plot the adsorption isotherms as a function of pressure, using data for the $\mu - P$ relationship from previous work[14]. The absolute isotherms are shown in the left panel of Fig. 4(c) and show an excellent agreement between the (μ, V, L) and (μ, V, T) simulation results and with prior work. To further assess the validity of the (μ, V, L) approach, we also compute the excess adsorption isotherm obtained using the excess number N^e of adsorbed Argon atoms calculated according to

$$N^e = N - V_{void}\rho_g \tag{19}$$

in which N is the absolute number of adsorbed Argon atoms computed during the simulations, V_{void} is the void (accessible) volume for the porous material[69,84], and ρ_g is the molar density of the gas phase in equilibrium with the adsorbed fluid. The excess adsorption

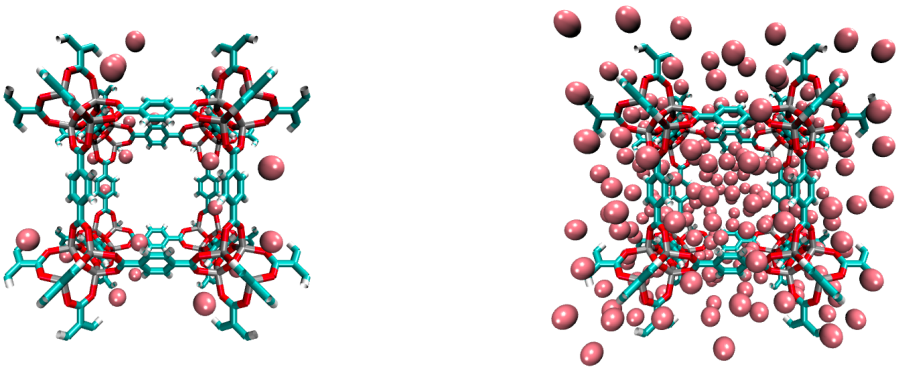

(a) (b)

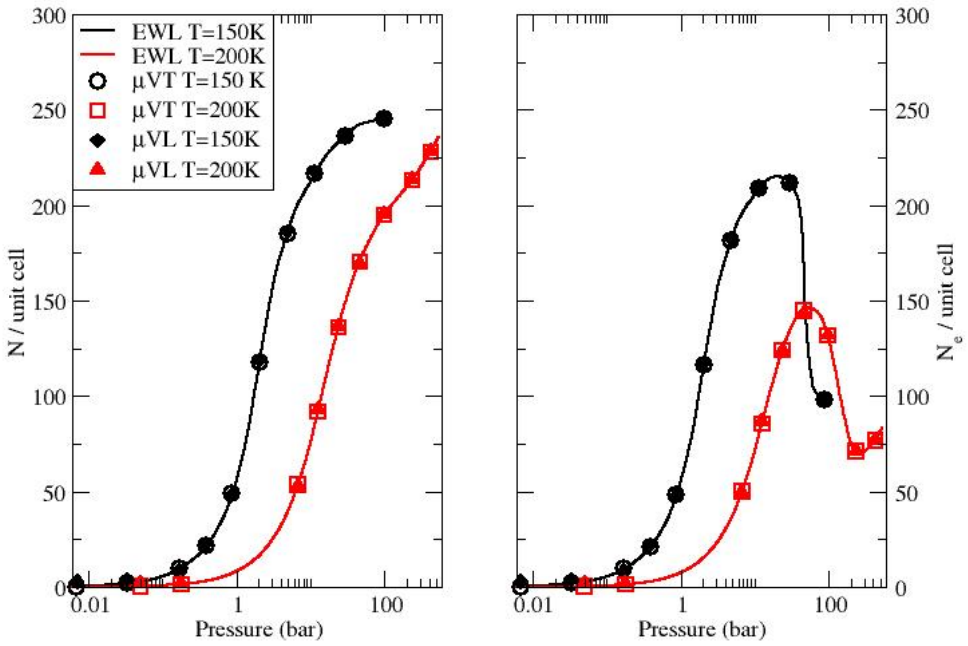

(c)

FIG. 4: (a and b) Argon adsorbed in IRMOF-1 at $T = 150$ K. Snapshot of a unit cell with Ar atoms adsorbed (shown as pink spheres) obtained during (μ, V, L) simulations for $\mu = -475$ kJ/kg and $L = 3.5 \times 10^4$ K (a) and for $\mu = -375$ kJ/kg and $L = 1.78 \times 10^5$ K (b). (c-Left) Absolute adsorption isotherms at $T = 150$ K and $T = 200$ K obtained in prior work using a flat-histogram method[15] (solid lines), μVT simulations (this work - open symbols), and μVL simulations (this work - filled symbols). (c-Right) Comparison between excess adsorption isotherms. The excess isotherms exhibit a maximum since adsorption takes place in the supercritical regime.

isotherms are shown in the right panel of Fig. 4(c). As discussed by Myers and Monson[84], the presence of a maximum in the excess isotherms indicates that the adsorption process takes place in the supercritical regime, thereby confirming that, under these conditions, there is no free energy barrier for the condensation undergone by the adsorbed fluid during adsorption. This means that the isothermal and adiabatic simulations both converge very quickly and thus provide a reliable self-consistency check. Furthermore, the plots show that there is an excellent agreement between the results obtained for the excess adsorption isotherms between the results from (μ, V, L) and (μ, V, T) simulation methods, and with prior work. Overall, this set of results establish the reliability of the (μ, V, L) simulation method for the prediction of adsorption isotherms in nanoporous materials.

C. Adsorption and Desorption in MCM-41

To explore the efficiency of the (μ, V, L) simulations and compare it to the (μ, V, T) simulations, we turn in this section to a system that has been shown previously to exhibit hysteresis[5,9,52], *i.e.*, the adsorption and desorption of Argon in MCM-41.

Peterson and Gubbins[80] previously located the conditions for liquid-vapor coexistence for this system at $T^* = 0.73$ and found a chemical potential at coexistence equal to $\mu^*_{coex} = -10.53$. At μ^*_{coex}, the confined fluid can coexist as a low-density (vapor) adsorbed phase and as a high-density (liquid) phase. Representative snapshots of these two phases obtained during (μ, V, L) simulations are shown for the low-density ($\mu^* < \mu^*_{coex}$) and high-density ($\mu^* > \mu^*_{coex}$) phases are shown in Figs. 5(a) and (b). Under isothermal conditions, the system exhibits hysteresis[5,52] over a range of chemical potentials bracketing μ^*_{coex} and shown in Fig. 5(c) as dotted lines. This can be seen by carrying out (μ, V, T) simulations runs starting from configurations that are initially empty (results labeled as Adsorption - μVT in Fig. 5(c)) or from a completely filled MCM-41 pore (results labeled as Desorption - μVT in Fig. 5(c)). As shown in Fig. 5(c), this leads to the formation of metastable states beyond the coexistence line for both the low-density→high-density and high-density→low-density transitions. This hysteresis is due to the free energy barrier of nucleation of liquid bridges during capillary condensation and of the free energy barrier of nucleation of vapor bubbles during capillary evaporation as shown in previous work[5,9,52]. As shown in Fig. 5, we observe an hysteresis in the onset of the low-density→high-density transition for μ^* up to about -10.4 (adsorption

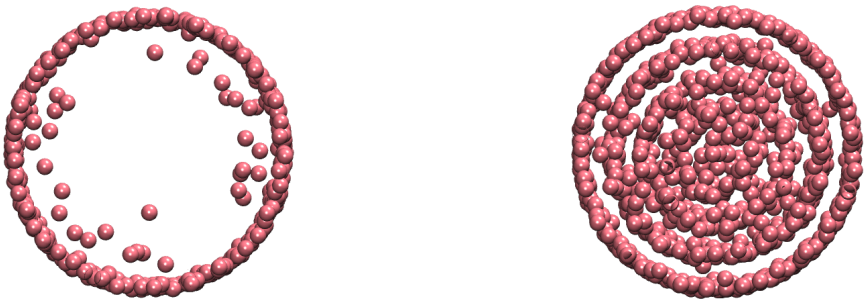

(a) (b)

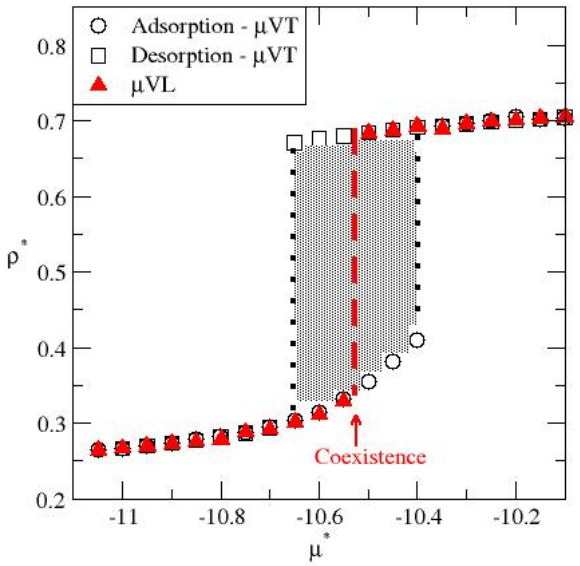

(c)

FIG. 5: (a and b) Argon adsorbed in MCM-41 at $T^* = 0.73$. The pore structure is omitted and only the adsorbed Ar atoms are shown as pink spheres. Snapshots taken during (μ, V, L) simulations in (a) for $\mu^* = -10.8$ and $L^* = 1709$ and in (b) for $\mu^* = -10.45$ kJ/kg and $L^* = 5083$. (c) Adsorption isotherms. Filled triangles are (μ, V, L) simulation results, open squares are (μ, V, T) simulation results obtained during desorption (starting from a completely filled MCM-41 pore) and open circles are (μ, V, T) simulation results obtained during adsorption (starting from an empty pore). Black dotted lines bracket the hysteresis region in gray, and the red dashed line is the coexistence line[80].

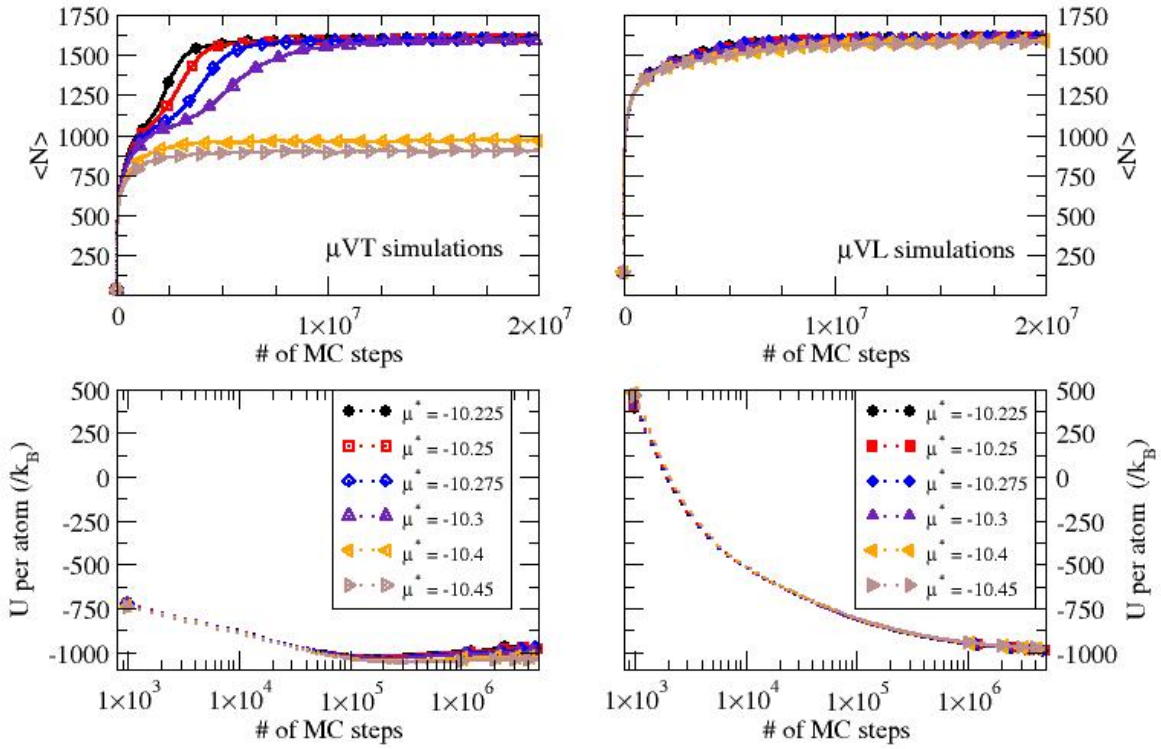

FIG. 6: Adsorption of Ar in MCM-41 at $T^* = 0.73$. Average number of atoms (top) and average potential energy per particles (bottom) collected over 75 realizations of MC runs of 2×10^7 MC steps each. The left panel shows results obtained for simulations in the (μ, V, T) ensemble while the right panel shows results for the corresponding (μ, V, L) simulations.

branch) and in the onset of the high-density→low-density transition for μ^* down to about -10.7 (desorption branch). On the other hand, we do not observe any hysteresis under adiabatic conditions and obtain a single loading curve regardless of the initial configurations used in the (μ, V, L) simulations. Adiabatic simulations thus provide a direct access to the equilibrium value for the loading for the entire range of chemical potentials without requiring the use of advanced and enhanced sampling simulation techniques[5,9,52].

To compare the efficiency of the (μ, V, T) and (μ, V, L) simulation methods, we examine the rate of convergence for the two approaches as μ^* approaches the hysteresis region. First, we start with the adsorption branch and collect averages over many realizations, *i.e.*.

simulation runs of 2×10^7 MC steps starting from an empty pore and a different sequence of random numbers. The results so obtained are presented in Fig. 6. Looking at the number of Argon atoms adsorbed in the pore (top panel of Fig. 6), we find that the rate of convergence of the simulations towards the high-density adsorbed phase for the (μ, V, T) simulations decreases as μ^* decreases from -10.225 to $-10.3$and approaches the hysteresis region. Furthermore, as the conditions enter the hysteresis region, the system remains in the low-density phase when μ^* is below -10.4 and becomes close to the coexistence value ($\mu^*_{coex} = -10.48$). On the other hand, the convergence of the (μ, V, L) simulations quickly occurs for all values of μ^*. The filling mechanisms are, however, markedly different as evidenced by the plots of the potential energy per particle (bottom panels of Fig. 6 - see also MovieS1 and MovieS2 in the supporting information). In the early stages of the (μ, V, T) simulations, the Ar atoms are all inserted at energetically favorable locations, resulting in a low potential energy per particle. On the other hand, early during the (μ, V, L) simulations, the adiabatic conditions allow atoms to be inserted at energetically unfavorable locations, leading to an initially positive potential energy per particle for all μ values. This enables the convergence of the (μ, V, L) simulations towards the equilibrium loading for conditions that are within the isothermal hysteresis region.

In line with what we observed for the bulk in Fig. 3, the average temperature overshoots the equilibrium value in the early stages of the simulation, thereby ensuring a faster equilibration than for (μ, V, T) simulations (see Fig. 7). To quantify this, we determine numerically the characteristic number of MC steps N_τ necessary to reach a loading greater than N_∞/e, where N_∞ is the equilibrium value for the loading. We plot N_τ against the supersaturation $\Delta\mu = \mu^* - \mu^*_{coex}$ for both sets of simulations. For (μ, V, T) simulations, N_τ increases as conditions approach coexistence and $\Delta\mu$ decreases. However, N_τ remains much lower and of the order of 1.2×10^6 steps for the (μ, V, L) simulations over the $\Delta\mu$ range, which further shows the efficiency of the adiabatic approach to predict the equilibrium isotherm.

We finally turn to the desorption process for Argon adsorbed in MCM-41 and show the results collected over a series of realizations, *i.e.* simulation runs of 20×10^7 MC steps using different configurations with a filled pore as starting points and different sequences of random numbers. The results obtained for the number of Argon atoms adsorbed in the pore are shown for the two simulation methods in the top panels of Fig. 8. In the case of the isothermal (μ, V, T) simulations, the rate of convergence towards the low-density

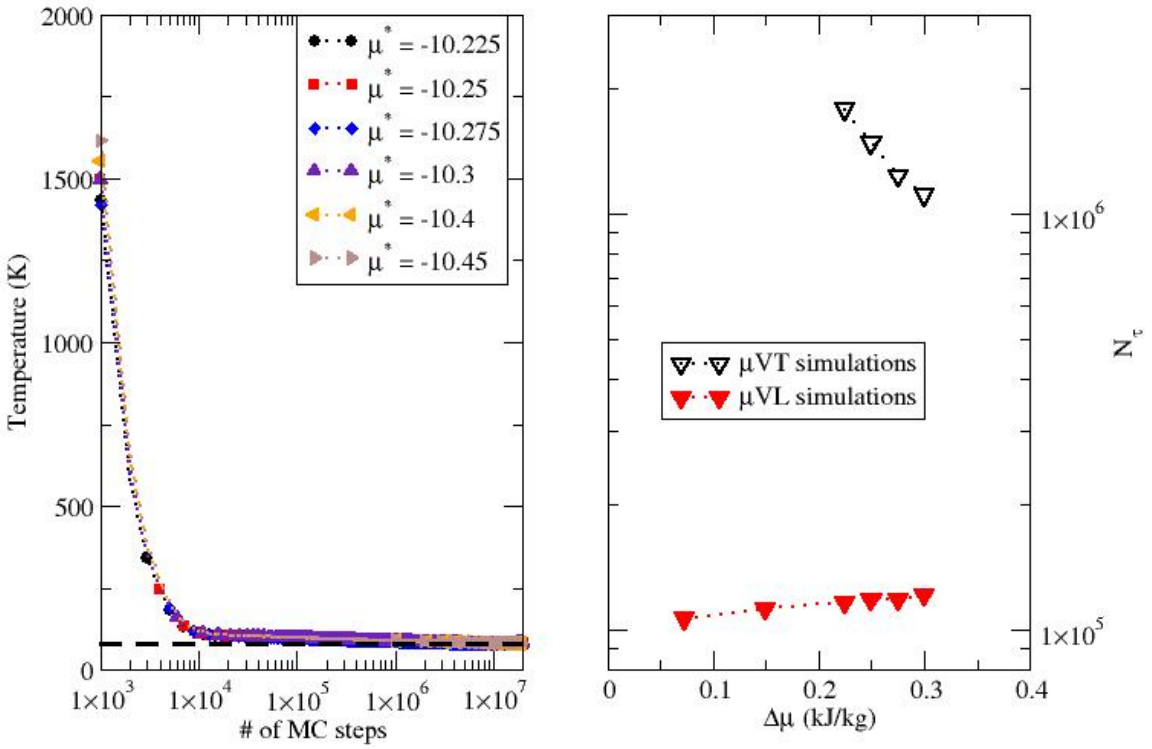

FIG. 7: Adsorption of Ar in MCM-41 at $T^* = 0.73$. (Left) Average temperature collected over 80 realizations of (μ, V, L) runs of 2×10^7 MC steps. The dashed line indicates the equilibrium temperature of $T^* = 0.73$ towards which all simulations converge.

adsorbed phase decreases as μ^* increases from -10.85 to -10.8, and the system remains in the high-density adsorbed phase when μ is within the isothermal hysteresis region and μ^* is close to the coexistence value. On the other hand, under adiabatic conditions, the convergence of the (μ, V, L) simulations towards the equilibrium value of the loading takes place more quickly than for isothermal simulations for all conditions and we do not observe any hysteresis. As provided in the Supplementary Material (MovieS3 and MovieS4), the emptying mechanisms are very different and account for the different kinetics observed. During isothermal simulations, emptying the pore involves the system overcoming a free energy barrier of nucleation of a capillary bubble as shown in Fig. 8(b). This is in agreement with findings from prior work under isothermal conditions[5,9]. Under adiabatic conditions,

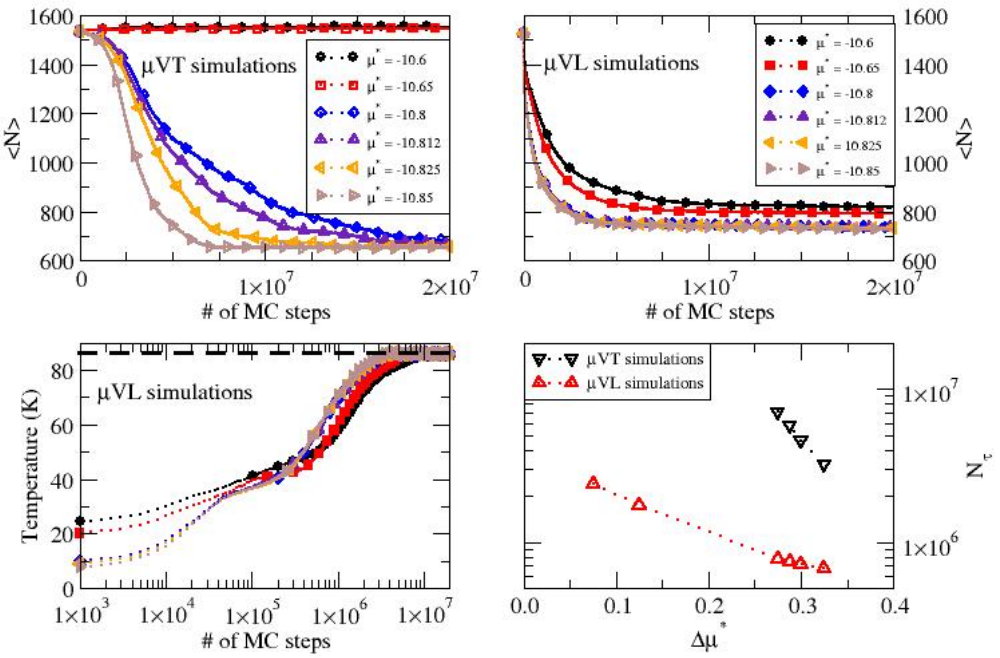

(a)

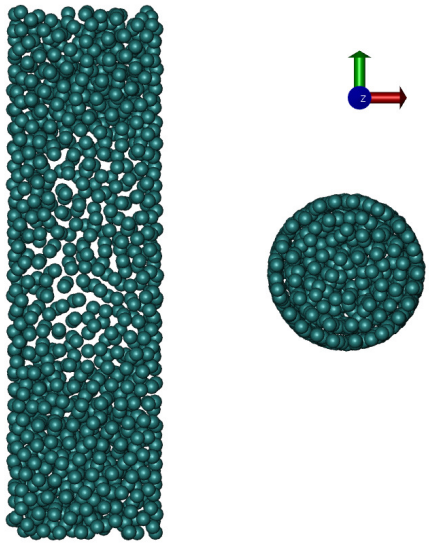

(b)

FIG. 8: (a) Desorption of Ar in MCM-41 at $T^* = 0.73$. Average number of atoms (μVT - top left, μVL - top right), average temperature (μVL - bottom left), and N_τ (both methods - bottom right) collected over 80 realizations of 2×10^7 MC steps. (b) Snapshot obtained after 1.8×10^7 MC steps of a realization of a desorption (μ, V, T) run at $\mu^* = -10.8$ showing the formation of a gas bubble on the left.

as can be seen on MovieS4, no such bubbles form and the pore quickly becomes empty. The temperature plot shown in the bottom left panel of Fig. 8(a) provides further insight into the efficiency of the adiabatic simulations. The initial configurations for the desorption runs consist of filled pores and out-of-equilibrium, *i.e.*, are effectively at a temperature much lower than the equilibrium temperature. As previously discussed, the temperature of the system can change during adiabatic simulations. As Argon atoms desorb, the temperature of the system increases (see Fig. 8(b)) and the system evolves towards equilibrium. When μ^* increases beyond -10.65 and approaches μ^*_{coex}, the initial temperature increases and becomes close to the equilibrium temperature. We find that its evolution towards the equilibrium value for the temperature is slower, resulting in an overall lower rate of convergence observed in the right panel of Fig. 8(b). We observe nonetheless, for all μ^* and supersaturation values, the adiabatic (μ, V, L) simulations converge towards the equilibrium loading, in sharp contrast with their isothermal (μ, V, T) counterparts.

V. CONCLUSIONS

In this work, we examine how adiabatic simulations can alleviate the impact of free energy barriers on the efficiency of isothremal simulations in bulk and nanoconfined systems. The main results from this work are as follows. We demonstrate the reliability of adiabatic simulations in the adiabatic grand-isochoric (μ, V, L) ensemble for adsorption processes through the example of the supercritical adsorption of Argon in the metal-organic framework IRMOF-1. This system, in which the supercritical conditions ensure that there is no free energy barrier, provides a benchmark to validate the first application of (μ, V, L) simulations to study adsorption in a nanoporous material. Results are found to be in excellent agreement with the adsorption isotherms predicted by the isothermal grand-canonical (μ, V, T) simulations and by flat-histogram methods[15], thereby establishing the reliability of the (μ, V, L) approach to predict adsorption properties. The results also show how the value for the Hill energy L that corresponds to a specific temperature can be rapidly interpolated and allow for a direct comparison with data obtained experimentally at a given T (see, it e.g., Fig. 1 for a plot of the $L - T$ interdependence. Furthermore, we provide a thorough asssessment of the efficiency of (μ, V, L) simulations, when compared to isothermal (μ, V, T) simulations, both in the bulk and in nanoconfined systems. In the bulk, we show that the

convergence rate of adiabatic simulations is essentially independent of the degree of supersaturation, while the convergence rate of isothermal simulations rapidly increases as the degree of supersaturation decreases, exhibiting a behavior expected for an activated process. Under nanoconfinement, we observe a similar behavior at high supersaturation. Moreover, at low supersaturation, isothermal simulations exhibit a strong hysteresis and remain in metastable states. On the other hand, adiabatic simulations converge towards the equilibrium state. We relate these results to the ability of adiabatic simulations to sample a wide range of temperature and potential energy. Thus, adiabatic simulation efficiently explore the configuration space and exhibit a faster convergence than isothermal simulations. Adiabatic (μ, V, L) simulations therefore provide a robust and efficient method that gives a direct and rapid access to the equilibrium loading and phase diagram under nanoconfinement when studying the adsorption and desorption of a fluid in a nanoporous material. The success and efficiency of adiabatic simulation methods could be especially useful in many practical cases such as, for instance, when performing a high-throughput screening of nanoporous materials for gas storage applications[18–26].

VI. SUPPLEMENTARY MATERIAL

Movies in .mp4 format are provided for the filling mechanism of MCM-41 under isothermal conditions (MovieS1) and under adiabatic conditions (MovieS2). We also provide movies for the emptying mechanism of MCM-41 under isothermal conditions (MovieS3) and under adiabatic conditions (MovieS4).

Acknowledgments

Partial funding for this research was provided by the National Science Foundation through award CHE-2240526. This work used the Open Science Grid through allocation TG-CHE210056 from the Advanced Cyberinfrastructure Coordination Ecosystem: Services & Support (ACCESS) program[85], which is supported by National Science Foundation grants

#2138259, #2138286, #2138307, #2137603, and #2138296.

---

[1] P. G. Debenedetti, *Metastable liquids: concepts and principles* (Princeton University Press, 2020).

[2] S. Auer and D. Frenkel, Nature **409**, 1020 (2001).

[3] C. Desgranges and J. Delhommelle, Phys. Rev. Lett. **123**, 195701 (2019).

[4] D. N. Theodorou, Ind. Eng. Chem. Res. **49**, 3047 (2010).

[5] A. Vishnyakov and A. V. Neimark, J. Chem. Phys. **119**, 9755 (2003).

[6] P. Ravikovitch, S. Ó. Domhnaill, A. Neimark, F. Schüth, and K. Unger, Langmuir **11**, 4765 (1995).

[7] M. Jorge and N. A. Seaton, Mol. Phys. **100**, 3803 (2002).

[8] J. Puibasset and R. J.-M. Pellenq, J. Chem. Phys. **122** (2005).

[9] C. Desgranges and J. Delhommelle, J. Chem. Phys. **146**, 184104 (2017).

[10] C. Desgranges and J. Delhommelle, Langmuir **35**, 15401 (2019).

[11] T. Horikawa, D. Do, and D. Nicholson, Adv. Colloid Interface Sci. **169**, 40 (2011).

[12] L. F. Velasco, R. Guillet-Nicolas, G. Dobos, M. Thommes, and P. Lodewyckx, Carbon **96**, 753 (2016).

[13] M. S. Shell, P. G. Debenedetti, and A. Z. Panagiotopoulos, Phys. Rev. E **66**, 056703 (2002).

[14] C. Desgranges and J. Delhommelle, J. Chem. Phys. **136**, 184107 (2012).

[15] C. Desgranges and J. Delhommelle, J. Chem. Phys. **136**, 184108 (2012).

[16] J. R. Errington, J. Chem. Phys. **118**, 9915 (2003).

[17] B. Mazur, L. Firlej, and B. Kuchta, ACS Appl. Mater. Interfaces (2024).

[18] Y. J. Colón and R. Q. Snurr, Chem. Soc. Rev. **43**, 5735 (2014).

[19] N. S. Bobbitt and R. Q. Snurr, Molec. Simul. **45**, 1069 (2019).

[20] A. Sturluson, M. T. Huynh, A. R. Kaija, C. Laird, S. Yoon, F. Hou, Z. Feng, C. E. Wilmer, Y. J. Colón, Y. G. Chung, et al., Molec. Simul. **45**, 1082 (2019).

[21] J. Vicent-Luna, A. Luna-Triguero, and S. Calero, J. Phys. Chem. C **120**, 23756 (2016).

[22] M. V. Parkes, C. L. Staiger, J. J. Perry IV, M. D. Allendorf, and J. A. Greathouse, Phys. Chem. Chem. Phys. **15**, 9093 (2013).

[23] R. B. Getman, Y.-S. Bae, C. E. Wilmer, and R. Q. Snurr, Chem. Rev. **112**, 703 (2012).

[24] M. Erdoôs, M. F. De Lange, F. Kapteijn, O. A. Moultos, and T. J. Vlugt, ACS Appl. Mater. Interfaces **10**, 27074 (2018).

[25] G. Ercakir, G. O. Aksu, and S. Keskin, J. Chem. Phys. **160** (2024).

[26] W. Park, K. H. Oh, D. Lee, S.-Y. Kim, and Y.-S. Bae, Chem. Eng. J. **452**, 139189 (2023).

[27] J. Haile and H. Graben, Mol. Phys. **40**, 1433 (1980).

[28] H. Graben and J. R. Ray, Phys. Rev. A **43**, 4100 (1991).

[29] J. R. Ray, Phys. Rev. A **44**, 4061 (1991).

[30] M. Lísal, M. Bendová, and W. R. Smith, Fluid Phase Equil. **235**, 50 (2005).

[31] L. D. Gelb and S. N. Chakraborty, J. Chem. Phys. **135**, 224113 (2011).

[32] F. A. Escobedo, J. Chem. Phys. **123** (2005).

[33] F. A. Escobedo, Phys. Rev. E **73**, 056701 (2006).

[34] L. Rosso, J. B. Abrams, and M. E. Tuckerman, J. Phys. Chem. B **109**, 4162 (2005).

[35] T. Cagin and B. M. Pettitt, Molec. Simul. **6**, 5 (1991).

[36] T. Kristóf and J. Liszi, Mol. Phys. **94**, 519 (1998).

[37] J. R. Ray and H. Graben, J. Chem. Phys. **93**, 4296 (1990).

[38] H. Graben and J. R. Ray, Mol. Phys. **80**, 1183 (1993).

[39] C. Desgranges and J. Delhommelle, J. Chem. Phys. **153**, 094114 (2020).

[40] P. Ströker and K. Meier, Phys. Rev. E **105**, 035301 (2022).

[41] I. Nitzke and J. Vrabec, J. Chem. Theory Comput. **19**, 3460 (2023).

[42] C. Desgranges and J. Delhommelle, J. Chem. Phys. **156**, 084113 (2022).

[43] E. Guggenheim, J. Chem. Phys. **7**, 103 (1939).

[44] T. L. Hill, *An introduction to statistical thermodynamics* (Dover Books, New York, 1986).

[45] C. Desgranges and J. Delhommelle, *Molecular Networking: Statistical Mechanics in the Age of AI and Machine Learning* (CRC Press, 2024).

[46] J. R. Ray, H. Graben, and J. Haile, J. Chem. Phys. **75**, 4077 (1981).

[47] T. Çağin and B. M. Pettitt, Mol. Phys. **72**, 169 (1991).

[48] T. Kristóf and J. Liszi, Chem. Phys. Lett. **261**, 620 (1996).

[49] P. Ströker and K. Meier, Phys. Rev. E **107**, 064112 (2023).

[50] R. Lustig, J. Chem. Phys. **109**, 8816 (1998).

[51] E. M. Pearson, T. Halicioglu, and W. A. Tiller, Phys. Rev. A **32**, 3030 (1985).

[52] A. V. Neimark, P. I. Ravikovitch, and A. Vishnyakov, J. Phys. Condens. Matt. **15**, 347 (2003).

[53] M. P. Allen and D. J. Tildesley, *Computer Simulation of Liquids* (Clarendon, Oxford, 1987).

[54] M. Eddaoudi, J. Kim, N. Rosi, D. Vodak, J. Wachter, M. O'Keeffe, and O. M. Yaghi, Science **295**, 469 (2002).

[55] O. M. Yaghi, M. O'Keeffe, N. W. Ockwig, H. K. Chae, M. Eddaoudi, and J. Kim, Nature **423**, 705 (2003).

[56] S. Kitagawa, R. Kitaura, and S.-i. Noro, Angew. Chem. Intl. Ed. **43**, 2334 (2004).

[57] S. Keskin, J. Liu, R. B. Rankin, J. K. Johnson, and D. S. Sholl, Ind. Eng. Chem. Res. **48**, 2355 (2009).

[58] T. Düren, Y.-S. Bae, and R. Q. Snurr, Chem. Soc. Rev. **38**, 1237 (2009).

[59] C. Desgranges and J. Delhommelle, Mol. Syst. Des. Eng. **6**, 52 (2021).

[60] S. S. Han, H. Furukawa, O. M. Yaghi, and W. A. I. Goddard, J. Am. Chem. Soc. **130**, 11580 (2008).

[61] P. J. Waller, F. Gándara, and O. M. Yaghi, Acc. Chem. Res. **48**, 3053 (2015).

[62] G. Garberoglio, A. I. Skoulidas, and J. K. Johnson, J. Phys. Chem. B **109**, 13094 (2005).

[63] G. Garberoglio, Langmuir **23**, 12154 (2007).

[64] H. Frost, T. Düren, and R. Q. Snurr, J. Phys. Chem. B **110**, 9565 (2006).

[65] K. S. Walton, A. R. Millward, D. Dubbeldam, H. Frost, J. J. Low, O. M. Yaghi, and R. Q. Snurr, J. Am. Chem. Soc. **130**, 406 (2008).

[66] M. De Toni, P. Pullumbi, F.-X. Coudert, and A. H. Fuchs, J. Phys. Chem. C **114**, 21631 (2010).

[67] J. M. Hicks, C. Desgranges, and J. Delhommelle, J. Phys. Chem. C **116**, 22938 (2012).

[68] A. R. V. Koenig, C. Desgranges, and J. Delhommelle, Molec. Simul. **40**, 71 (2014).

[69] J. A. Greathouse, T. L. Kinnibrugh, and M. D. Allendorf, Ind. Eng. Chem. Res. **48**, 3425 (2009).

[70] D. Banerjee, C. M. Simon, A. M. Plonka, R. K. Motkuri, J. Liu, X. Chen, B. Smit, J. B. Parise, M. Haranczyk, and P. K. Thallapally, Nat. Commun. **7**, 1 (2016).

[71] A. I. Skoulidas and D. S. Sholl, J. Phys. Chem. B **109**, 15760 (2005).

[72] Q. Yang and C. Zhong, J. Phys. Chem. B **110**, 17776 (2006).

[73] D. Dubbeldam, C. J. Galvin, K. S. Walton, D. E. Ellis, and R. Q. Snurr, J. Am. Chem. Soc. **130**, 10884 (2008).

[74] Y. He, W. Zhou, G. Qian, and B. Chen, Chem. Soc. Rev. **43**, 5657 (2014).

[75] K. Gopalsamy, C. Desgranges, and J. Delhommelle, J. Phys. Chem. C **121**, 24692 (2017).

[76] C. Desgranges and J. Delhommelle, J. Phys. Chem. C **124**, 1907 (2020).

[77] S. L. Mayo, B. D. Olafson, and W. A. Goddard, J. Phys. Chem. **94**, 8897 (1990).

[78] Y. Liu, D. Liu, Q. Yang, C. Zhong, and J. Mi, Ind. Eng. Chem. Res. **49**, 2902 (2010).

[79] C. Desgranges and J. Delhommelle, J. Chem. Phys. **140**, 104109 (2014).

[80] B. K. Peterson and K. E. Gubbins, Mol. Phys. **62**, 215 (1987).

[81] A. Vishnyakov and A. V. Neimark, Langmuir **19**, 3240 (2003).

[82] A. V. Neimark and A. Vishnyakov, J. Chem. Phys. **122** (2005).

[83] P. Ravikovitch, D. Wei, W. Chueh, G. Haller, and A. Neimark, J. Phys. Chem. B **101**, 3671 (1997).

[84] A. Myers and P. Monson, Langmuir **18**, 10261 (2002).

[85] T. J. Boerner, S. Deems, T. R. Furlani, S. L. Knuth, and J. Towns, in *Practice and Experience in Advanced Research Computing* (Association for Computing Machinery, New York, NY, USA, 2023), PEARC '23, p. 173–176, ISBN 9781450399852, URL `https://doi.org/10.1145/3569951.3597559`.